

# Stripe order and vibrational properties of $\text{La}_2\text{NiO}_{4+\delta}$ for $\delta=2/15$ : Measurements and *ab initio* calculations

C. C. Homes\* and J. M. Tranquada

*Condensed Matter Physics & Materials Science Department, Brookhaven National Laboratory, Upton, New York 11973, USA*

D. J. Buttrey

*Department of Chemical Engineering, University of Delaware, Newark, Delaware 19716, USA*

(Received 18 August 2006; revised manuscript received 1 December 2006; published 26 January 2007)

The optical properties of the static charge- and stripe-ordered material  $\text{La}_2\text{NiO}_{4+\delta}$  for  $\delta=\frac{2}{15}$  have been measured over a wide frequency and temperature range for light polarized within the *a-b* planes and along the *c* axis. Below the charge-ordering temperature,  $T_{\text{co}}\approx 319$  K, a charge gap opens and the electronic background, upon which four strong infrared-active phonons are superimposed, drops towards zero. As the temperature decreases, many new spectral features are observed in response to the ordering of interstitial oxygen as well as the formation of a superlattice due to the charge order in the  $\text{NiO}_2$  planes. In particular, the prominent mode at  $354\text{ cm}^{-1}$  splits into three components; while the frequencies do not shift below the magnetic-ordering transition at  $T_{\text{m}}=110$  K, there is a transfer of oscillator strength in response to the change in registry of the charge stripes with respect to the underlying lattice. *Ab initio* calculations have been performed using density-functional theory, and the phonon dispersion curves were obtained using the direct method. Likely assignments of the new modes activated by stripe order are discussed. In some crystals, two antiresonances are observed in the conductivity for  $T\approx T_{\text{co}}$ , which change to a resonant character for  $T\lesssim T_{\text{m}}$ ; these modes are shown to be due to longitudinal optic *c*-axis modes which appear as a result of surface misorientation.

DOI: [10.1103/PhysRevB.75.045128](https://doi.org/10.1103/PhysRevB.75.045128)

PACS number(s): 63.20.Dj, 71.15.Mb, 71.45.Lr, 78.30.-j

## I. INTRODUCTION

Unusual ordered states are observed when holes are doped into two-dimensional transition-metal oxides. The existence of charge-stripe order and incommensurate magnetism in the layered nickelates<sup>1-7</sup> and certain cuprates<sup>8</sup> is now fairly well established. One system that has received a great deal of attention is  $\text{La}_{2-x}\text{Sr}_x\text{NiO}_4$ , a compound that is isostructural with superconducting cuprates.<sup>6,9-22</sup> The substitution of Sr for La dopes holes into the  $\text{NiO}_2$  planes ( $n_h=x$ ). In particular, for  $\text{La}_{1.67}\text{Sr}_{0.33}\text{NiO}_4$  a charge-ordering transition is observed<sup>23,24</sup> at  $T_{\text{co}}\approx 240$  K. Below the charge-ordering transition dramatic changes occur in the electronic and vibrational spectra of this material.<sup>15,18,25</sup> It has been established by neutron and x-ray-diffraction studies that the holes in the  $\text{NiO}_2$  planes tend to order into charge stripes, separating antiferromagnetic (AFM) domains.<sup>1,4-7</sup> However, the stripe order in these systems exists only over a finite range.

The oxygen-doped nickelate system  $\text{La}_2\text{NiO}_{4+\delta}$  for  $\delta=\frac{2}{15}$  provides a useful comparison with the Sr-doped systems. Previous optical studies have focused mainly on the stoichiometric  $\text{La}_2\text{NiO}_4$  system,<sup>26-29</sup> while studies of the oxygen-doped materials are limited.<sup>30</sup> The excess oxygens sitting at interstitial sites are three-dimensionally ordered,<sup>5</sup> and they dope holes ( $n_h=2\delta$ ) into the  $\text{NiO}_2$  planes. The holes are observed to order into diagonal stripes that exhibit long-range, three-dimensional order.<sup>1,5,31</sup> Measurements of the in-plane resistance suggest that the stripe and interstitial orderings appear simultaneously at  $T_{\text{co}}\approx 317$  K, an unusually high temperature for stripe order in the nickelates,<sup>32</sup> while the magnetic ordering occurs at a much lower temperature  $T_{\text{m}}=110$  K.

In this paper we examine the optical properties and the infrared-active vibrations of  $\text{La}_2\text{NiO}_{4.133}$  ( $\delta=\frac{2}{15}$  doping) over

a wide frequency and temperature range for light polarized in the  $\text{NiO}_2$  planes and along the insulating *c* axis. The electronic and transport properties of this material have been discussed previously.<sup>32</sup> While the vibrational spectrum for  $T\lesssim T_{\text{co}}$  is relatively simple, for  $T\lesssim T_{\text{m}}$  there is a great deal of vibrational fine structure in the planes. In particular, the in-plane mode at  $\approx 354\text{ cm}^{-1}$  splits into three modes, and there is a redistribution of spectral weight between 90 K and  $T_{\text{m}}$ . The redistribution correlates with the shift in character of the stripes, as identified by neutron-diffraction studies.<sup>5</sup> To better understand the nature of the lattice vibrations, *ab initio* calculations have been performed using density-functional theory; the phonon dispersion curves were obtained using the direct method assuming a simple tetragonal unit cell. The formation of a superlattice due to the charge order in the system, as well as the general reduction of symmetry due to the presence of interstitial oxygen, appears sufficient to explain the splitting of the  $354\text{-cm}^{-1}$  mode, as well as the appearance of many other new vibrational features.

In some crystals, two modes were observed which appeared as antiresonances in the *a-b* plane optical conductivity, and are shown to have a strong polarization dependence and to correspond to the location of the longitudinal optic modes of the infrared-active *c*-axis vibrations. Model calculations indicate that the antiresonances observed in this material are due to sample misorientation and are not intrinsic features associated with stripe order.

## II. EXPERIMENT

The single crystals studied here were grown by radio-frequency skull melting.<sup>33</sup> After orienting the crystal by x-ray Laue diffraction, a surface was cut perpendicular to the

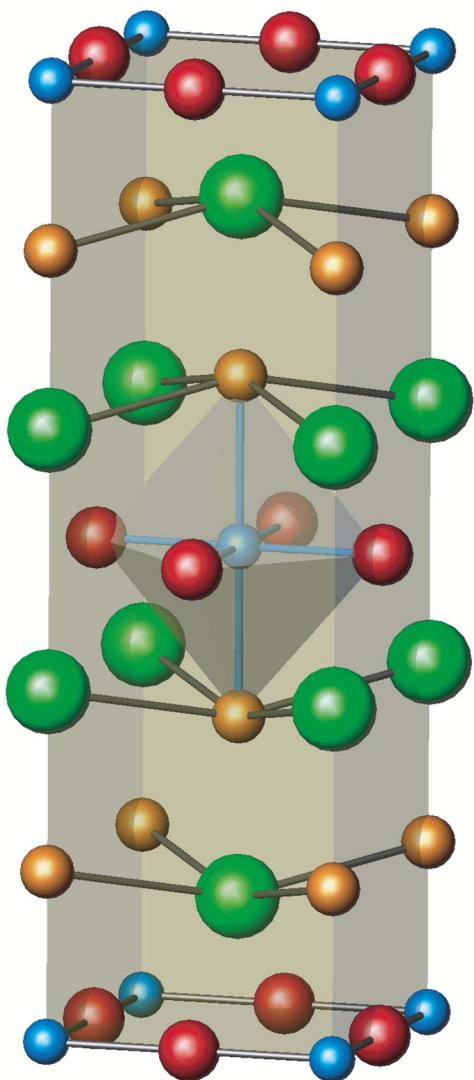


FIG. 1. (Color online) The unit cell of  $\text{La}_2\text{NiO}_4$  in the tetragonal  $I4/mmm$  setting with  $a=b=3.888 \text{ \AA}$  and  $c=12.555 \text{ \AA}$ . The  $\text{NiO}_2$  layers are separated by  $\text{LaO}$  bilayers. There are two different oxygen environments; the oxygen atoms in the  $\text{NiO}_2$  planes are referred to in the text as O(1), while the apical oxygen atoms in the  $\text{LaO}$  layers are referred to as O(2).

$c$  axis (parallel to the  $\text{NiO}_2$  planes) and then polished. Subsequently, the oxygen concentration was selected by annealing at  $464 \text{ }^\circ\text{C}$  for 5 days in flowing  $\text{O}_2$  (1 bar), followed by a quench to room temperature. The annealing conditions were chosen to give a nominal  $\delta$  of 0.133, based on earlier work on the phase diagram.<sup>33</sup>

The structure of  $\text{La}_2\text{NiO}_4$  as an ideal body-centered tetragonal  $I4/mmm$  phase is shown in Fig. 1. The actual structure at room temperature has a lower symmetry due to tilts of the  $\text{NiO}_6$  octahedra about  $[110]$  axes; the resulting unit cell is orthorhombic, with a doubled volume.<sup>27,34–36</sup> When excess oxygen atoms are added, they go to interstitial sites located between the  $\text{LaO}$  bilayers,<sup>34</sup> with the site occupancies correlated with the octahedral tilt pattern.<sup>37</sup> In  $\text{La}_2\text{NiO}_{4+\delta}$  with  $\delta = \frac{2}{15}$ , the interstitials order three dimensionally,<sup>31</sup> with a unit cell of size  $3\sqrt{2}a \times 5\sqrt{2}a \times 5c$  relative to the tetragonal cell

of Fig. 1. Although the model for interstitial order has orthorhombic symmetry, no orthorhombic splitting of Bragg peaks has been detected by neutron diffraction.

Resistivity and magnetization measurements have been performed on a portion of the single crystal examined here.<sup>32</sup> There are two small jumps in the resistivity, the first at the magnetic ordering temperature of  $T_m=110 \text{ K}$ , and the second at  $T_{co}=317 \text{ K}$ , which seems to correspond with both charge and interstitials ordering. The charge-ordering temperature observed in  $\text{La}_{2-x}\text{Sr}_x\text{NiO}_4$  for  $x=0.275$ , close to the hole concentration of our sample, is considerably lower ( $T_{co} \approx 190 \text{ K}$ ). Detailed structure in both the resistivity and magnetization below  $T_m$  correspond to lock-in transitions of the ordered states of the interstitial oxygens.<sup>5</sup>

For the infrared measurements, the crystal was mounted on an optically black cone and cooled in an open-flow cryostat. The temperature dependence of the reflectance for light polarized in the  $a$ - $b$  planes and along the  $c$  axis was measured at a near-normal angle of incidence from  $\approx 20$  to over  $26\,000 \text{ cm}^{-1}$  using an *in situ* overcoating technique.<sup>38</sup> Previous studies of crystals with similar oxygen contents revealed little temperature dependence in the high-frequency reflectance.<sup>32</sup> Consequently, in this work the reflectance above  $12\,000 \text{ cm}^{-1}$  has been assumed to be temperature independent. The optical conductivity has been determined from a Kramers-Kronig analysis of the reflectance, for which extrapolations are necessary for  $\omega \rightarrow 0, \infty$ . At low frequency, a metallic extrapolation,  $R \propto 1 - \omega^{1/2}$ , was used for  $T \gtrsim 180 \text{ K}$ ; at lower temperatures the reflectance was assumed to continue smoothly to  $\approx 0.55$  at zero frequency. At high frequency, the reflectance was assumed to be constant from the highest measured point to  $1 \times 10^5 \text{ cm}^{-1}$ , above which a free-electron approximation ( $R \propto \omega^{-4}$ ) was assumed.

### III. RESULTS

#### Optical properties

The unpolarized  $ab$ -plane reflectance of  $\text{La}_2\text{NiO}_{4.133}$  from  $\approx 20$  to over  $12\,000 \text{ cm}^{-1}$  is shown in Fig. 2 at a variety of temperatures both above and below the magnetic ordering transition,  $T_m=110 \text{ K}$ . At room temperature, the low-frequency reflectance is tending towards unity, indicating the sample is somewhat metallic in nature. The reflectance in the midinfrared is somewhat higher than previously reported values.<sup>30</sup> However, the low-frequency reflectance decreases rapidly with temperature, characteristic of a metal-to-insulator transition and the formation of a charge gap. While the magnitude of the reflectance does not change dramatically below  $T_m$ , there is a continuous evolution of fine structure in the reflectance from room temperature down to  $10 \text{ K}$ ; this structure becomes considerably sharper below  $T_m$ .

The reflectance for light polarized along the poorly conducting  $c$  axis has been measured over the same frequency range at a variety of temperatures; data in the region of the lattice vibrations are shown in the inset of Fig. 2. The  $c$ -axis reflectance is dominated by the infrared-active lattice vibrations (characteristic of an insulator) and is similar in nature to  $c$ -axis measurements done on lightly doped  $\text{La}_{2-x}\text{Sr}_x\text{NiO}_4$ .<sup>10</sup>

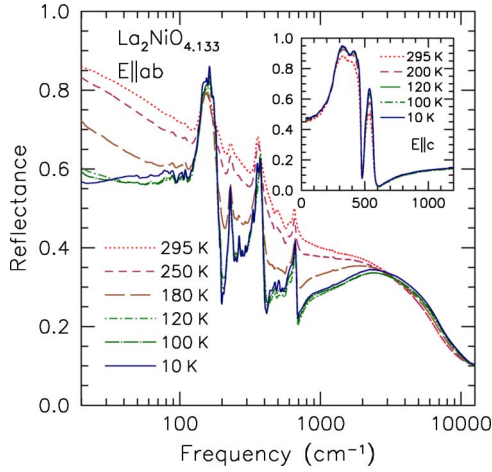


FIG. 2. (Color online) The reflectance for light polarized in the  $a$ - $b$  planes of  $\text{La}_2\text{NiO}_{4.133}$  shown from  $\approx 20 \text{ cm}^{-1}$  to over  $12\,000 \text{ cm}^{-1}$  at a variety of temperatures above and below  $T_m = 110 \text{ K}$ . The reflectance at low frequency drops quickly with decreasing temperature in response to the formation of a charge gap. At low temperature the reflectance is typical of an insulator and is dominated by the infrared-active modes; below  $T_m$  a great deal of vibrational fine structure develops. Inset: The temperature-dependent reflectance of  $\text{La}_2\text{NiO}_{4.133}$  for light polarized along the  $c$  axis.

In addition to the rich vibrational structure observed in the  $a$ - $b$  planes, some crystals also displayed unusual features in the reflectance that show up as antiresonances in the conductivity at  $\approx 470$  and  $560 \text{ cm}^{-1}$  (asterisks in Fig. 3). Interestingly, at low temperature where the conductivity is suppressed, these features tend to disappear (or to revert to a normal resonant line shape, in data not shown). Features such as these have been previously observed, to a greater or lesser extent, in virtually all studies of nickelates<sup>13,15,21,30</sup> and

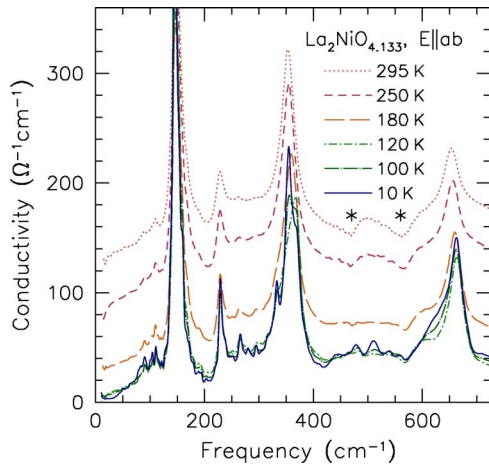


FIG. 3. (Color online) The temperature dependence of the optical conductivity in the region of the infrared-active lattice vibrations for  $\text{La}_2\text{NiO}_{4.133}$  for  $E||ab$ . The weak antiresonances attributed to the  $c$ -axis LO modes are denoted by asterisks. The reduction of the electronic background with decreasing temperature signals the formation of a charge gap. In addition, there is a great deal of fine structure below  $T_m$ .

cuprates,<sup>39–46</sup> where the samples are oriented, cut, and then polished. This effect, while interesting, is attributable to the  $c$ -axis longitudinal optic modes which are activated due to the misorientation of the sample, as discussed in more detail in the Appendix.

The temperature dependence of the optical conductivity for light polarized in the  $a$ - $b$  planes is shown in the region of the infrared-active vibrations in Fig. 3. At room temperature, the material appears to be weakly metallic, with  $\sigma_{dc} \equiv \sigma_1(\omega \rightarrow 0) \approx 120 \Omega^{-1} \text{ cm}^{-1}$ . There are four strong vibrations at  $150$ ,  $229$ ,  $354$ , and  $654 \text{ cm}^{-1}$  superimposed on an electronic background that decreases with temperature as the charge gap develops;<sup>32</sup> in addition to these modes, the two antiresonances previously mentioned are faintly visible at room temperature (indicated by the asterisks in Fig. 3), but weakened as the electronic background decreases. The decrease in the low-frequency optical conductivity below  $T_{co}$  is accompanied by a commensurate increase in the conductivity in the midinfrared region; this shift in spectral weight has been previously examined by us.<sup>32</sup> There is also a great deal of fine structure in Figs. 2 and 3 that evolves continuously below room temperature, becoming particularly sharp for  $T \lesssim T_m$ . The conductivity along the  $c$ -axis is entirely due to two strong vibrations at  $265$  and  $507 \text{ cm}^{-1}$ . Unlike the in-plane conductivity shown in Fig. 3, the  $c$ -axis conductivity shows little temperature dependence or fine structure.

The features in the conductivity have been fit using a model for the complex dielectric function,  $\tilde{\epsilon}(\omega) = \epsilon_1(\omega) + i\epsilon_2(\omega)$ , which consists of a series of Lorentzian oscillators:

$$\tilde{\epsilon}(\omega) = \epsilon_\infty + \sum_j \frac{\omega_{p,j}^2}{\omega_j^2 - \omega^2 - i\gamma_j\omega}, \quad (1)$$

where  $\omega_j$ ,  $\gamma_j$ , and  $\omega_{p,j}$  are the frequency, width, and effective plasma frequency of the  $j$ th vibration;  $\epsilon_\infty$  is the high-frequency contribution to the dielectric function. The complex conductivity is related to the dielectric function by  $\tilde{\sigma}(\omega) = \sigma_1(\omega) + i\sigma_2(\omega) = -2\pi i\omega[\tilde{\epsilon}(\omega) - \epsilon_\infty]/Z_0$  (where  $Z_0 = 377 \Omega$  is the impedance of free space); when vibrational parameters are expressed in  $\text{cm}^{-1}$  the conductivity has the units  $\Omega^{-1} \text{ cm}^{-1}$ . When taken with a linear background (to approximate the electronic contribution), this simple model describes the data quite well. The results of the fits to the vibrational features at room temperature and  $10 \text{ K}$  are listed in Table I. Note that for light polarized in the  $a$ - $b$  planes there are at least 32 vibrational features observed at low temperature; Table I only lists 20 of them, so it is by no means exhaustive.

## IV. ANALYSIS AND DISCUSSION

### A. Vibrational features associated with stripe order

As indicated in Table I, the in-plane conductivity at room temperature is dominated by four modes. These can be interpreted by ignoring the superstructure and considering just the expected modes for the body-centered-tetragonal cell of Fig. 1. The irreducible vibrational representations for the  $I4/mmm$  space group are

TABLE I. The vibrational parameters for oscillator fits to the conductivity of  $\text{La}_2\text{NiO}_{4.133}$  for light polarized in the  $a$ - $b$  planes and along the  $c$  axis at 295 and 10 K, where  $\omega_j$ ,  $\gamma_j$ , and  $\omega_{p,j}$  are the frequency, width, and effective plasma frequency of the  $j$ th vibration. While there are at least 32 vibrational features observed at 10 K; only the 20 strongest features are listed. All units are in  $\text{cm}^{-1}$ , except for the dimensionless oscillator strength  $S_j = \omega_{p,j}^2 / \omega_j^2$ .

$E \parallel ab$							
295 K				10 K			
$\omega_j$	$\gamma_j$	$\omega_{p,j}$	$(S_j)$	$\omega_j$	$\gamma_j$	$\omega_{p,j}$	$(S_j)$
654	38	365	(0.31)	663	23	369	(0.31)
				633	47	313	(0.24)
				539	7.9	46	(0.05)
				511	15	112	(0.06)
				478	11	80	(0.03)
354	28	498	(1.97)	369	15	258	(0.48)
				354	15	401	(1.28)
				331	16	196	(0.35)
				319	12	90	(0.08)
				295	5.2	55	(0.04)
				281	5.6	48	(0.03)
				266	5.2	83	(0.10)
				251	5.2	37	(0.08)
				237	5.3	67	(0.15)
				229	5.8	166	(0.52)
229	13	171	(0.55)	220	6.0	40	(0.03)
				160	6.8	160	(1.00)
				150	18	514	(11.7)
150	18	514	(11.7)	146	10	506	(12.0)
				111	3.1	59	(0.28)
				105	4.7	50	(0.22)
				89	4.1	55	(0.38)
$E \parallel c$							
295 K				10 K			
507	29	263	(0.26)	506	18	250	(0.24)
265	32	1167	(19.4)	269	25	1160	(18.6)

$$2A_{1g} + 2E_g + 3A_{2u} + B_{2u} + 4E_u,$$

where four doubly degenerate  $E_u$  modes are expected to be infrared active in the  $a$ - $b$  planes;<sup>21,47</sup> the  $B_{2u}$  mode is silent, and the  $A_{2u}$  modes are active along the  $c$  axis. The  $g$  modes are Raman active only.

To identify the nature of the vibrational modes, one requires a model of the lattice vibrations. Pintschovius *et al.*<sup>47</sup> fit phonon dispersions, measured by inelastic neutron scattering on  $\text{La}_2\text{NiO}_4$ , with a modified rigid ion model (and later with a shell model<sup>48</sup>). From their analysis, the mode at  $654 \text{ cm}^{-1}$  involves Ni-O(1) bond-stretching motion of the in-plane oxygens, while the  $354\text{-cm}^{-1}$  mode involves Ni-O(1) bond-bending motion of the in-plane oxygens. (The equivalent modes in  $\text{La}_2\text{NiO}_4$  are at  $660$  and  $353 \text{ cm}^{-1}$ , for  $T = 70 \text{ K}$ .) The two lower modes involve motions of the Ni and La ions against the apical oxygens; these tend to be sensitive to rotations and distortions of the  $\text{NiO}_6$  octahedra, and are of less interest to us.

The increases in the unit-cell size due to interstitial order and due to stripe order are expected to introduce new infrared-active modes. The larger unit cell in real space results in a smaller Brillouin zone in reciprocal space. Folding the phonon branches into the first Brillouin zone increases the number of modes at  $q=0$ , a fraction of which will be IR active.

Some of the lower-energy modes identified at 10 K in Table I, such as those at  $89$ ,  $111$ , and  $266 \text{ cm}^{-1}$ , are still present weakly at room temperature; hence these are likely associated with interstitial order, which is fully established below  $250 \text{ K}$ .<sup>31</sup> We will focus here on the modes that change significantly at lower temperatures, especially below  $T_m$ , where the charge-order parameter abruptly increases.<sup>5</sup>

The most dramatic changes are associated with the mode at  $354 \text{ cm}^{-1}$ , which develops an increasing asymmetry with decreasing temperature until three modes, at  $331$ ,  $354$ , and  $369 \text{ cm}^{-1}$ , become clearly visible at  $T_m$ . The detailed temperature dependence of these modes is shown in Figs. 4(a)

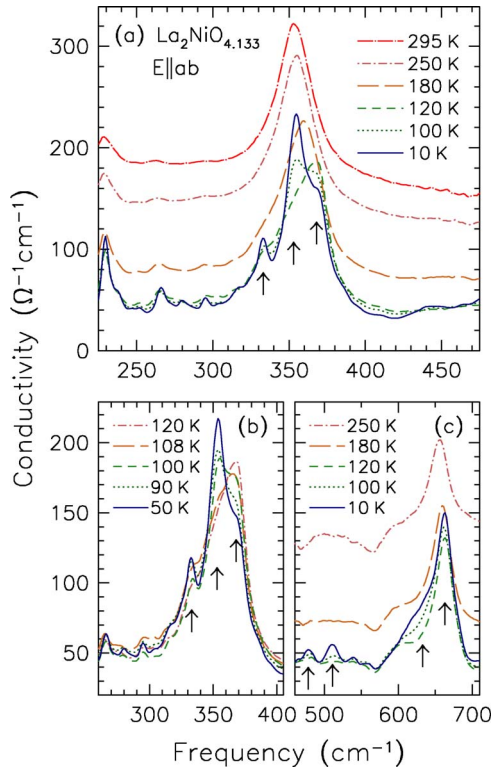


FIG. 4. (Color online) (a) The real part of the optical conductivity in the region of the vibration at  $354 \text{ cm}^{-1}$ . At room temperature, the vibration appears as a single mode. At  $\approx 180 \text{ K}$  the mode has a pronounced asymmetry and some additional weak features in the conductivity are also discernible. Below the magnetic transition at  $T_m = 110 \text{ K}$  the asymmetry is resolved as the vibration splits into a three modes at  $332$ ,  $354$ , and  $369 \text{ cm}^{-1}$  (arrows). (b) The detailed temperature dependence of the modes close to  $T_m$ . (c) The temperature dependence of the mode at about  $660 \text{ cm}^{-1}$ , which develops a shoulder at about  $630 \text{ cm}^{-1}$  below  $T_m$ , as well as additional fine structure at  $478$  and  $511 \text{ cm}^{-1}$ .

and 4(b), with the latter showing the behavior close to  $T_m$ . An apparent splitting of the Ni-O(1) bond-bending mode is commonly observed in Sr-doped nickelates in association with stripe and checkerboard order,<sup>15,16,22,49,50</sup> although the situation has been less clear in O-doped nickelates.<sup>30,51</sup> The unusual feature in our case is that the weights of the three peaks change significantly on cooling through  $T_m$ . In addition, while the Ni-O(1) bond-stretching mode hardens slightly on cooling, a shoulder at  $633 \text{ cm}^{-1}$  grows up below  $T_m$ , as seen in Fig. 4(c). Looking on a finer scale, one can also see the appearance below  $T_m$  of peaks at  $478$  and  $511 \text{ cm}^{-1}$ ; these correspond precisely to the strong  $A_{1g}$  modes detected by Raman scattering in the stripe-ordered phase of Sr-doped nickelates.<sup>18,21,25</sup>

The fitted frequencies and relative weights of the three peaks in the bond-bending regime are shown in Figs. 5(a) and 5(b) below  $180 \text{ K}$ ; above this temperature it is increasingly difficult to obtain a meaningful three-peak fit. The dimensionless oscillator strength ( $S_j = \omega_{p,j}^2 / \omega_j^2$ ) of the  $354\text{-cm}^{-1}$  mode at  $295 \text{ K}$  is  $\approx 2$ , while the sum of the oscillator strengths of the three modes at  $10 \text{ K}$  is  $\approx 2.1$ , indicating that the oscillator strength is approximately conserved. The

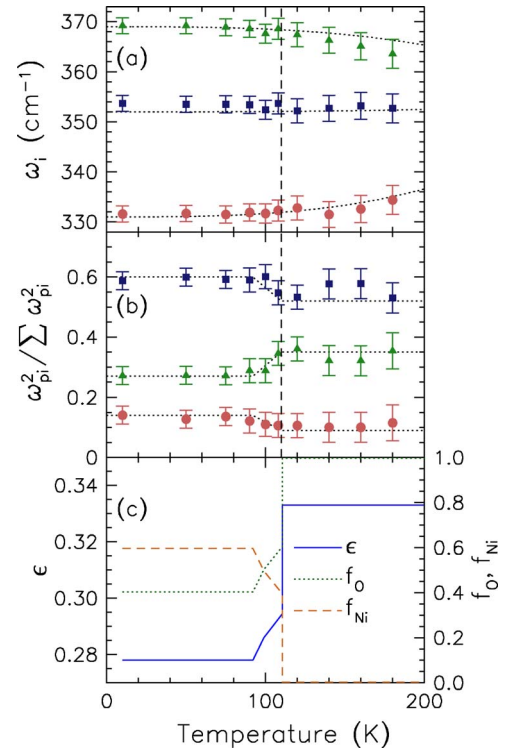


FIG. 5. (Color online) Temperature dependence of the (a) frequencies and (b) relative intensities of the three peaks identified in Figs. 4(a) and 4(b). The dashed line denotes  $T_m = 110 \text{ K}$ ; the dotted lines are guides to the eye. (c) Temperature dependence of the charge stripe incommensurability,  $\epsilon$ , and the fractions of O-centered,  $f_O$ , and Ni-centered,  $f_{Ni}$ , stripes.

temperature dependence of the intensities of these modes relative to the total intensity of all three, i.e.,  $\omega_{p,j}^2 / \sum_j \omega_{p,j}^2$ , is shown in Fig. 5(b). The relative intensities show little temperature dependence for  $T \geq T_m$ ; however, for  $90 \text{ K} \leq T \leq T_m$  there is a rapid redistribution of oscillator strength between the three modes. The  $354\text{-}$  and  $331\text{-cm}^{-1}$  modes increase in intensity through this transition, while the  $369\text{-cm}^{-1}$  mode decreases in intensity; below  $90 \text{ K}$  there is again no change in the relative intensities.

The variation in the relative intensities shown in Fig. 5(b) is correlated with a first-order transition in the stripe ordering at  $T_m$ . To describe the latter, we first need to introduce the wave vector for charge order within an  $\text{NiO}_2$  plane, which can be written as  $\mathbf{q}_{co} = (\epsilon, \epsilon, 0)$ . For  $T > T_m$ ,  $\epsilon = \frac{1}{3}$  due to locking of the charge stripes to a second harmonic of the interstitial order. Magnetic ordering induces a discontinuous jump in  $\epsilon$ , together with a substantial increase in the order parameter associated with charge order. Below  $T_m$ ,  $\epsilon$  changes continuously, with some lock-in plateaus, down to  $\sim 90 \text{ K}$ , and it stays relatively constant below that.<sup>5</sup> The approximate variation of  $\epsilon$  is indicated by the solid line in Fig. 5(c).

An important issue in stripe physics concerns the registry of the stripes with respect to the lattice. In this particular case, it has been argued on the basis of the response to a uniform magnetic field<sup>52</sup> and from analysis of harmonic intensities<sup>5</sup> that the charge stripes are centered on rows of O atoms for  $T > T_m$ ; they shift towards Ni-centering on cooling

TABLE II. Theoretical and experimental lattice constants and atomic fractional coordinates for the optimized structure of  $\text{La}_2\text{NiO}_4$  for the tetragonal  $I4/mmm$  space group (14 atoms in the unit cell, four nonequivalent displacive particles).

	Theory (LDA)		Experiment <sup>a</sup>
	Unconstrained	Constrained	
$a$ (Å)	3.702	3.796	3.888
$c$ (Å)	12.867	12.252	12.555
$c/a$	3.47	3.23	3.23
La (0 0 $z$ )	0.3627	0.3727	0.3636
Ni (0 0 0)			
O(1) ( $0 \frac{1}{2} 0$ )			
O(2) (0 0 $z$ )	0.1811	0.1768	0.1793
Ni-O(1) (Å)	1.85	1.90	1.94
La-O(2) (Å)	2.68	2.73	2.79

<sup>a</sup>The in-plane lattice constant for the  $I4/mmm$  unit cell has been determined from the lattice constants in orthorhombic  $Bmab$  by assuming  $(a+b)/(2\sqrt{2})$ , listed in Ref. 34.

below  $T_m$ . The estimated relative fractions of O-centered ( $f_O$ ) and Ni-centered stripes ( $f_{Ni}$ ) are indicated, respectively, by the long-dashed and short-dashed lines in Fig. 5(c), where  $f_O = (4\epsilon - 1)/\epsilon$  and  $f_{Ni} = (1 - 3\epsilon)/\epsilon$ .

The correlations between the relative intensities of the phonon peaks and the stripe character suggest that the IR phonon intensities contain information about the stripe registry. To extract information on the stripe registry from the IR phonon relative intensities, we need to know the contributions of different atomic sites to each observable phonon. In pursuit of that information, we have resorted to a first-principles calculation of the lattice dynamics, which we describe in the next section.

## B. Calculation of phonon modes

### 1. Approach

The phonon frequencies were determined from first principles using the direct method,<sup>54</sup> in which the dynamical matrix is derived from the Hellmann-Feynman force constants arising when a single atom is displaced from its equilibrium position. The forces are calculated using density-functional theory. The calculations were limited to the  $I4/mmm$  space group, with 14 atoms in the unit cell.

The initial step in this procedure is to determine the equilibrium volume and geometry for which the forces on each atom in the unit cell are minimized. The *ab initio* calculations on  $\text{La}_2\text{NiO}_4$  were performed using the full potential linearized augmented plane wave (FP-LAPW) method<sup>55</sup> with local orbital extensions<sup>56</sup> in the WIEN2K implementation.<sup>57</sup> The local-density approximation (LDA) exchange-correlation potential was used. Studies with different Monkhorst-Pack  $k$ -point meshes indicated that a  $5 \times 5 \times 5$  mesh was sufficient for good energy convergence. Two different strategies were employed for geometry optimization. The first approach is to allow the volume and  $c/a$  ratio of the

unit cell to vary without constraint while minimizing the total energy; the second approach is to vary the volume but constrain the  $c/a$  ratio to equal the experimentally observed value. Further geometric optimization was achieved by refining the atomic fractional coordinates within the unit cell until the total force on each of the atoms is typically less than 0.1 mRy/au. The results of the volume and geometry optimization are summarized in Table II. The constrained optimization yields values for the lattice constants that are in reasonable agreement with the experimentally observed values;<sup>34</sup> the full optimization leads to a unit cell that is compressed in the  $a$ - $b$  plane and elongated along the  $c$  axis, resulting in shorter Ni-O(1) bonds. For this reason, the geometry determined from the constrained method has been utilized, and the calculated total energy vs volume is illustrated in Fig. 6. A bulk modulus of 199 GPa is extracted by fitting to the Murnaghan equation of state.<sup>53</sup>

### 2. Zone-center modes

To determine the phonons at the zone center, a  $1 \times 1 \times 1$  supercell is sufficient. To obtain a complete set of Hellmann-Feynman forces, a total of nine independent displacements are required; we have considered symmetric displacements, which doubles this number, resulting in 18 separate structure files. In this case, displacement amplitudes of 0.03 Å were used. Typical values for the displacements range from 0.02 to 0.06 Å; however, the displacements should be small enough to ensure that the response is still linear. In this study we examined several smaller values for the displacements and observed no change in the results; we therefore concluded that 0.03 Å was an acceptable value. The introduction of displacements also has the effect of lowering the symmetry of the system. For these calculations a  $7 \times 7 \times 2$   $k$ -point mesh was chosen. After each structure has converged using the criteria that the total forces on each atom are less than

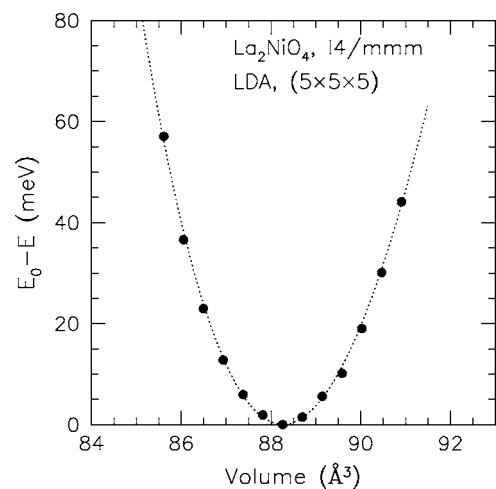


FIG. 6. Calculated total energy for the formula unit  $\text{La}_2\text{NiO}_4$  in the  $I4/mmm$  space group as a function of volume with constant  $c/a$  ratio. The calculated equilibrium volume of  $88.3 \text{ \AA}^3$  per formula unit is in good agreement with experimental value of  $94.8 \text{ \AA}^3$  (Ref. 34). The dotted line is a fit to the Murnaghan equation of state (Ref. 53).

TABLE III. Comparison of observed and calculated phonon frequencies (at 10 K) and relative intensities (angled brackets) of the four in-plane  $E_u$  modes ( $\mathbf{q}=0$ ) for  $\text{La}_2\text{NiO}_4$  in the tetragonal  $I4/mmm$  setting. Frequencies are expressed in  $\text{cm}^{-1}$ . The character of the mode is illustrated by the atomic intensities, shown to the first two significant figures.

$\omega_{obs}$	$E_u(\mathbf{q}=0)$			Atomic intensity			
	$\langle\omega_{p,j}^2\rangle$	$\omega_{calc}$	$\langle\mu_{ab}^2\rangle$	La	Ni	O(1)	O(2)
663	0.53	681	0.62	0.00	0.17	0.83	0.00
354	0.63	365	0.75	0.01	0.08	0.90	0.01
229	0.11	201	0.08	0.07	0.47	0.15	0.31
146	1.00	110	1.00	0.23	0.13	0.04	0.60

0.01 mRy/au, the residual forces are collected for each set of symmetric displacements and a list of the Hellmann-Feynman forces are generated. Using the program PHONON,<sup>58</sup> the cumulative force constants deconvoluted from the Hellmann-Feynman forces are introduced into the dynamical matrix, which is then diagonalized in order to obtain the phonon frequencies.

The calculated  $E_u$  phonon frequencies for  $\mathbf{q}=0$  are compared with the corresponding infrared-active vibrations observed at low temperature in Table III; with the exception of the two low-frequency modes, which are sensitive to octahedral tilts and distortions, the agreement between the *ab initio* values and the observed modes is excellent. The intensities have been estimated by calculating the net dipole moment of the atomic displacements

$$\mu_i = \sum_j Z_j^* w_{ij}, \quad (2)$$

where  $Z_j^*$  is the Born effective charge of the  $j$ th atom in the unit cell, and  $w_{ij}$  is its displacement in the  $i$ th direction. The square of each sum is considered to estimate the relative intensity for light polarized in the direction of that axis. In this instance,  $Z_j^*$  is simply assumed to be the full ionic charge for each atom. The relative intensities are listed in Table III and are found to be in good agreement with the experimentally measured quantities (proportional to the square of the effective plasma frequency  $\omega_{p,j}^2$ ). The atomic intensity is also listed (this quantity is the sum of the square of the vibrational amplitude of each atom over the allowed degrees of freedom). The atomic intensity characterizes the nature of the vibration. The eigenvectors of these four calculated  $E_u$  modes are in agreement with the previous analysis by Pintschovius *et al.*<sup>47</sup>

It is worth noting at this point that the high-frequency  $E_u$  mode is extremely sensitive to the Ni-O(1) bond length. The unconstrained optimization results in a relatively short Ni-O(1) bond (Table II), which in turn yields a value for the high-frequency  $E_u$  mode of  $\sim 750 \text{ cm}^{-1}$ . The constrained optimization results in slightly larger value for the Ni-O(1) bond length, and subsequently in a frequency closer to what is observed experimentally. For this reason, as well as those stated earlier, the constrained optimization is the preferred method.

### 3. Phonon dispersions and analysis of stripe-induced features

The accurate determination of phonon energies at finite  $\mathbf{q}$  requires the use of supercells. A  $2 \times 2 \times 1$  supercell with 56 atoms and a slightly reduced  $3 \times 3 \times 1$   $k$ -point mesh was chosen. A total of nine independent displacements (18 symmetric displacements) were again considered. The phonon frequencies have been determined using the method described in the previous section. The values for the  $E_u$  modes at  $\mathbf{q}=0$  determined by this method are within a few  $\text{cm}^{-1}$  of the previously determined values (Table III); 681, 361, 195, and  $107 \text{ cm}^{-1}$ .

The calculated phonon dispersion curves are shown in Fig. 7 along the high-symmetry  $\Gamma \rightarrow M$  direction in the region of the two infrared-active  $E_u$  modes. The results are in reasonable agreement with neutron-scattering data<sup>47,48</sup> (although the highest-energy LO branch is probably not correct in detail, as neutron scattering<sup>59</sup> has revealed anomalous behavior in  $\text{La}_{1.69}\text{Sr}_{0.31}\text{NiO}_4$ ). A purely covalent system has been assumed, so the transverse optic (TO) and longitudinal optic (LO) modes are degenerate at the zone center. As previously discussed, the charge order in the system results in the formation of a superlattice with the modulation wave vector  $\mathbf{q}_{co}$ ; the position of  $\mathbf{q}_{co}$  for  $T > T_m$ , where  $\epsilon = \frac{1}{3}$ , is indicated by the dotted line in Fig. 7, while the range of variation for  $T < T_m$  is indicated by the shaded region. New zone-center modes are expected to be folded back from the  $\mathbf{q}_{co}$  point.

The  $E_u(\mathbf{q}=0)$  Ni-O(1) bond-bending mode at  $354 \text{ cm}^{-1}$  appears to split into three features at low temperature. We expect that these should correspond to the original  $\mathbf{q}=0$  mode, plus two at  $\mathbf{q}=\mathbf{q}_{co}$  made IR-active by the charge order. In Fig. 7, one can see that the TO and LO branches that disperse from the  $E_u(\mathbf{q}=0)$  mode reach somewhat lower and higher frequencies at  $\mathbf{q}_{co}$ ,  $325$  and  $366 \text{ cm}^{-1}$  from Table IV. These seem likely to correspond to the two stripe-induced modes. We can also see from the table that the character of these  $\mathbf{q}=\mathbf{q}_{co}$  modes is different from that at  $\mathbf{q}=0$ : both have a substantially greater contribution from the apical oxygens, and the lower mode has a substantial contribution from Ni.

Given the differing characters of the three modes, the shift in relative intensities below  $T_m$  [Fig. 5(b)] in correspondence with the shift in character of the stripes seems quite reasonable. To get a better understanding of the connection between the phonon character and the stripe registry will require a calculation with a much larger cell that includes the details of

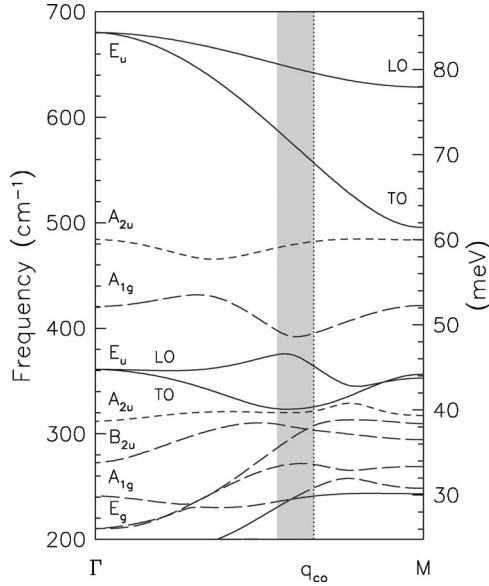


FIG. 7. The calculated phonon dispersion curves in  $\text{La}_2\text{NiO}_4$  for the tetragonal  $I4/mmm$  space group along the high-symmetry  $\Gamma \rightarrow M$  direction (zone diagonal), shown in the region of the two infrared-active  $E_u$  modes (solid lines). The transverse optic (TO) and longitudinal optic (LO) branches of the  $E_u$  modes are labeled. The  $A_{2u}$  modes (active along the  $c$  axis) are denoted by short-dashed line, while the remaining modes that are active in the  $a$ - $b$  planes are denoted by long-dashed lines. New zone-center modes are expected to be folded back from the  $\mathbf{q}_{\text{co}}$  branch point (dotted line); the range of variation of  $\epsilon$  for  $T < T_m$  is indicated by the shaded region [see Fig. 5(c)].

the charge order. While such a calculation is beyond the scope of the present study, it does appear to be feasible.

The shoulder detected at  $633 \text{ cm}^{-1}$  for  $T < T_m$  clearly must be associated with the Ni-O(1) bond-stretching mode at  $\mathbf{q}_{\text{co}}$ , as there are no other phonons that are close. It is worthwhile noting that the intensity of this feature is weaker than the activated bond-bending modes discussed above.

The weak features that are activated below  $T_m$  at  $478$  and  $511 \text{ cm}^{-1}$  correspond to strong Raman-active  $A_{1g}$  modes that are observed at low temperature in Sr-doped nickelates.<sup>18,21,25</sup> The  $A_{1g}(\mathbf{q}=0)$  mode involves only O(2)

displacements along the  $c$  axis and is calculated to be at  $421 \text{ cm}^{-1}$  (Table IV), which is close to the value of  $445 \text{ cm}^{-1}$  observed in undoped  $\text{La}_2\text{NiO}_4$ .<sup>28</sup> The  $A_{2u}(\mathbf{q}=0)$  mode calculated at  $484 \text{ cm}^{-1}$  looks like a better frequency match; however, it corresponds to the infrared-active  $c$ -axis mode that we observe at  $506 \text{ cm}^{-1}$  (Table I). Powder-diffraction studies<sup>34,60</sup> indicate that the Ni-O(2) bond length decreases with doping; that, together with the presence of oxygen interstitials, is likely to raise the  $A_{1g}$  branch. Thus it appears that the two observed features must correspond to modes with substantial Ni-O(2) bond-stretching character, consistent with the conclusion of Blumberg *et al.*<sup>18</sup> from their Raman study of  $\text{La}_{1.67}\text{Sr}_{0.33}\text{NiO}_4$ . In a similar Raman study, Yamamoto *et al.*<sup>25</sup> argued that both modes must be activated; however, given the strong Raman activity of the modes and the relative flatness of the  $A_{1g}$  and  $A_{2u}$  modes, it is not clear how or why Raman scattering would see two strong modes from  $\mathbf{q}=\mathbf{q}_{\text{co}}$  and none from  $\mathbf{q}=0$ . While the  $A_{1g}(\mathbf{q}=0)$  mode involves displacements only along the  $c$  axis, at  $\mathbf{q}=\mathbf{q}_{\text{co}}$  both in-plane and out-of-plane displacements are present. Furthermore, the  $A_{1g}$  mode, as well as many others, may also couple to the stripe order in the system leading to induced or enhanced dipole moments and IR activity in the planes.<sup>61</sup>

## V. CONCLUSIONS

The dominant in-plane vibrational properties of  $\text{La}_2\text{NiO}_{4.133}$  detectable in the optical conductivity near  $T_{\text{co}}$  are relatively simple, with just four strong modes. Considerable fine structure appears due to the ordering of interstitial oxygens and development of charge stripe order. The most prominent change occurs to the Ni-O(1) bond-bending mode at  $354 \text{ cm}^{-1}$ , which appears to split into three features at low temperature. On cooling through  $T_m$ , where there is a first-order transition due to the onset of magnetic order, a shift occurs in the charge-ordering wave vector, and a change occurs in the stripe registry with respect to the  $\text{NiO}_2$  planes; there is no shift in the frequencies of the three modes, however, there is a substantial redistribution of oscillator strength among the modes, indicating that the relative intensities contain useful information about the positions of the charge stripes in the lattice. Several other vibrational modes acti-

TABLE IV. Comparison of the calculated frequencies and atomic intensities of some of the high-frequency modes at the zone center and at the  $\mathbf{q}_{\text{co}}$  cut along the  $\Gamma \rightarrow M$  direction (Fig. 7) for the  $2 \times 2 \times 1$  supercell. The notation  $u$  and  $l$  denote the upper and lower branches of the doubly degenerate zone-center  $E_u$  modes. Frequencies are expressed in  $\text{cm}^{-1}$ .

Mode	$\omega_{\text{calc}}$	$\Gamma$				Branch	$\omega_{\text{calc}}$	$\mathbf{q}_{\text{co}}$			
		La	Ni	O(1)	O(2)			La	Ni	O(1)	O(2)
$E_u$	681	0.00	0.17	0.83	0.00	$E_u(u)$	643	0.00	0.07	0.91	0.03
						$E_u(l)$	559	0.00	0.14	0.86	0.00
$A_{2u}$	484	0.01	0.00	0.35	0.64	$A_{2u}$	482	0.00	0.01	0.56	0.43
$A_{1g}$	421	0.00	0.00	0.00	1.00	$A_{1g}$	395	0.01	0.01	0.20	0.78
$E_u$	361	0.02	0.07	0.90	0.01	$E_u(u)$	366	0.05	0.05	0.43	0.47
						$E_u(l)$	325	0.04	0.40	0.26	0.31
$A_{2u}$	312	0.10	0.06	0.57	0.27	$A_{2u}$	321	0.04	0.36	0.38	0.22
$B_{2u}$	272	0.00	0.00	1.00	0.00	$B_{2u}$	304	0.00	0.06	0.70	0.24

vated by the stripe order have also been identified.

*Ab initio* calculations were performed using density-functional theory to obtain the phonon dispersion curves for the tetragonal unit cell ( $I4/mmm$  space group) characterizing the average lattice structure, ignoring the modulations. The calculations do quite well at matching the strong  $\mathbf{q}=0$  modes. Likely assignments for the activated modes, occurring at  $\mathbf{q}=\mathbf{q}_{co}$ , have been discussed. It appears that a calculation with a full stripe-ordered unit cell should be feasible; this would allow a proper evaluation of the intensities of activated modes. In any case, it is apparent that the significant activated modes are associated with the Ni-O(1) bond-bending and bond-stretching phonon branches, and that they do not surpass the original  $\mathbf{q}=0$  modes in oscillator strength. These results may have relevance for attempts to identify stripe-induced features in studies of some cuprate compounds.

A detailed analysis of both the  $a$ - $b$  plane and  $c$  axis infrared-active vibrations has revealed that the antiresonances sometimes observed in the  $a$ - $b$  plane reflectance and optical conductivity are, in fact, due to the  $c$ -axis LO modes. These modes are observed as a result of either sample misalignment, surface roughness, or a combination of both, and have been previously observed to some extent in virtually all cuprate and nickelate systems where the samples have been cut and subsequently polished.

#### ACKNOWLEDGMENTS

We would like to thank T. Timusk for suggesting the possibility of  $c$ -axis LO modes appearing in the in-plane optical properties. We would also like to thank D. N. Basov, M. Braden, W. Ku, Y. Pashkevich, V. Perebeinos, L. Pintschovius, and M. Strongin for helpful discussions. This work was supported by the Office of Science, U.S. Department of Energy (DOE), under Contract No. DE-AC02-98CH10886; D.J.B. acknowledges support from DOE under Contract No. DE-FG02-00ER45800.

#### APPENDIX: BERREMAN MODES

In the study of this class of materials, it has been noted that some crystals displayed unusual antiresonances in the reflectance and conductivity at  $\approx 470$  and  $560\text{ cm}^{-1}$ ; in fact, there is even a hint of weak structure at these locations in Figs. 2 and 3. The presence of long-range charge and spin-stripe order in this material initially suggested that the peculiar line shapes of these two features may have been a result of Fano antiresonances of phonon modes with the electronic conductivity.<sup>21</sup> To test this possibility, a careful polarization study of the reflectance in the  $a$ - $b$  planes was undertaken, the results of which are shown in Fig. 8. The two features at  $\approx 470$  and  $560\text{ cm}^{-1}$  do indeed have a very strong polarization dependence, while the other features associated with the normally active infrared vibrations exhibit little or no dependence upon the polarization. As Fig. 8 indicates, an angle  $\theta_0$  may be chosen where the two antiresonant line shapes are completely removed; these features are most pronounced at  $\theta_0 + \frac{\pi}{2}$ , yet are again completely absent at  $\theta_0 + \pi$ . (Note that

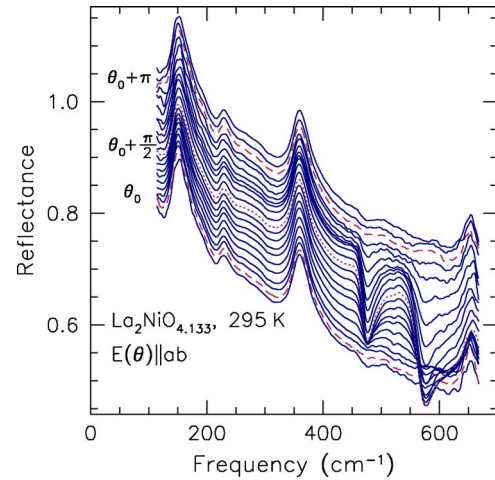


FIG. 8. (Color online) The reflectance of  $\text{La}_2\text{NiO}_{4.133}$  at room temperature in the region of the two low-frequency antiresonances for light polarized within the  $a$ - $b$  planes. A polarization angle  $\theta_0$  (dashed line) has been identified where the antiresonance features are totally absent from the reflectance spectra. These features are most pronounced at  $\theta_0 + \frac{\pi}{2}$  (dotted line); by  $\theta_0 + \pi$  (dash-dotted line) they have once again been totally removed from the reflectance.

$\theta_0$  depends upon the orientation of the sample, and does not correspond to either the  $s$  or  $p$  polarization of the instrument.) In the highly unlikely case that the sample contained a single domain of stripe order, the polarization dependence might indicate a Fano antiresonance correlated with the stripe modulation; however, a subsequent neutron-diffraction check of the crystal indicated that there was a slight misorientation of the  $a$ - $b$  face ( $\sim 10^\circ$ ).<sup>62</sup> This raised the very significant possibility of a  $c$ -axis contribution to the optical properties. The temperature dependence of the optical properties along the  $c$  axis have been measured, and the two strong features observed at room temperature in the optical conductivity at  $265$  and  $507\text{ cm}^{-1}$ , which sharpen at low temperature (Table I). These modes correspond to the TO modes of the infrared-active vibrations. However, the positions of these modes do not correspond to the location of the antiresonances. On the other hand, there are two prominent features in the  $c$ -axis loss function  $-\text{Im}[1/\tilde{\epsilon}_c(\omega)]$  which also sharpen at low temperature but which do not shift in frequency; these modes correspond to the LO vibrations of the infrared active modes, and the positions of these modes correspond almost *exactly* with the positions of the antiresonances in Fig. 8. Thus the  $c$ -axis properties do appear to be affecting the  $ab$ -plane optical properties via the  $c$ -axis LO modes.

For analysis of the optical properties, the nickelate structure may be treated as that of a uniaxial crystal. The complex Fresnel reflection coefficients for the  $s$  and  $p$  polarizations of a uniaxial crystal with the  $c$  axis oriented perpendicular to the surface of reflection are<sup>40,42,63,64</sup>

$$\tilde{r}_s = \frac{\cos \theta - \sqrt{\tilde{n}_{ab} - \sin^2 \theta}}{\cos \theta + \sqrt{\tilde{n}_{ab} - \sin^2 \theta}},$$

$$\tilde{r}_p = \frac{\tilde{n}_{ab}\tilde{n}_c \cos \theta - \sqrt{\tilde{n}_c^2 - \sin^2 \theta}}{\tilde{n}_{ab}\tilde{n}_c \cos \theta + \sqrt{\tilde{n}_c^2 - \sin^2 \theta}}, \quad (\text{A1})$$

where  $\theta$  is the angle of incidence, and  $\tilde{n}_{ab} = \tilde{n}_a = \tilde{n}_b$  and  $\tilde{n}_c$  are the complex refractive indices ( $\tilde{n} = n + ik$ ) in the  $a$ - $b$  planes and along the  $c$  axis, respectively. Note that the  $c$ -axis component enters only into  $\tilde{r}_p$ . Given the estimated misorientation of the  $a$ - $b$  planes of at least  $10^\circ$  and an angle of incidence in reflectance that varies between  $\sim 5^\circ$  and  $20^\circ$ , then the angle of incidence with respect to the  $a$ - $b$  planes may be as large as  $30^\circ$  for certain polarization angles.

The optical properties have been modeled using the values for the oscillators from Table I, as well as a free-carrier Drude component (an oscillator centered at zero frequency) to model the weakly metallic behavior in the planes.<sup>65</sup> The results for  $R_s$  ( $=\tilde{r}_s\tilde{r}_s^*$ ) and  $R_p$  ( $=\tilde{r}_p\tilde{r}_p^*$ ) at  $\theta=0^\circ$  and  $30^\circ$  are shown in Fig. 9(a); for comparison, the room temperature-experimental data are shown in Fig. 9(b). As noted,  $R_s$  has no structure associated with the  $c$  axis, while  $R_p$  has two prominent antiresonances. These antiresonances are not related to the normally infrared active TO vibrations along the  $c$  axis, but are instead related to the LO modes seen in the loss function. The peaks in the  $c$ -axis loss function coincide exactly with the antiresonant structures in the reflectance. This model describes the general features of the experimental data shown in Fig. 9(b) quite well (although the magnitude of the antiresonances is not exactly reproduced), including a slight reduction of the reflectance for  $E \parallel \theta_0 + \frac{\pi}{2}$ . These antiresonances have also been observed in cuprate systems,<sup>39–46</sup> and are referred to colloquially as Berreman modes.<sup>66</sup>

The antiresonances in the reflectance also appear as antiresonances in the electronic continuum, which evolve into resonances with decreasing temperature and the removal of the electronic background. A similar prominent antiresonance has previously been observed in the conductivity of  $\text{La}_{1.775}\text{Sr}_{0.225}\text{NiO}_4$  at  $\approx 577 \text{ cm}^{-1}$ ;<sup>21</sup> however, that feature displayed relatively little temperature dependence. It now seems clear that the antiresonance features in the reflectance and the conductivity are not due to coupling to the charge order in the system, but are instead a result of the misorientation of the  $a$ - $b$  plane, as well as other possible surface effects due to polishing. The polarization dependence of these features reflects the fact that different polarizations probe different

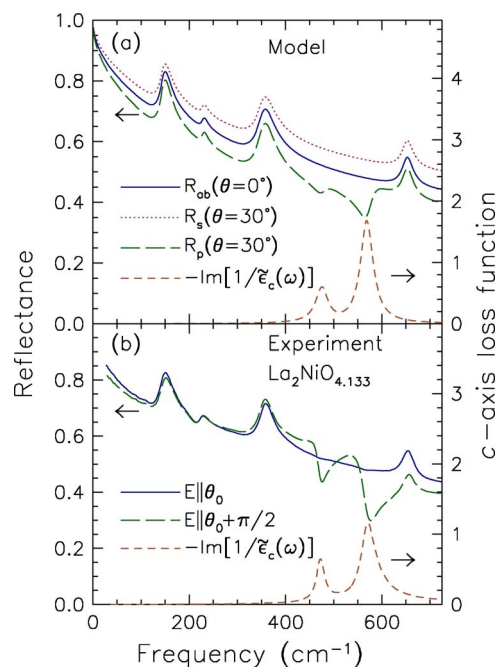


FIG. 9. (Color online) Model calculations. (a) The normal reflectance of the bulk (solid line) based on the experimentally determined oscillator parameters at room temperature for the  $ab$ -plane and  $c$ -axis (Table I) lattice modes, as well as the  $s$  and  $p$  polarized reflectance assuming a  $\theta=30^\circ$  angle of incidence (dotted and dashed lines, respectively). The  $c$ -axis loss function (short-dashed line) has two prominent peaks which correspond to the frequencies of the LO modes; these peaks correspond exactly with the antiresonance dips in the reflectance spectra for  $p$ -polarized light. (b) The experimentally determined room-temperature reflectance for  $\text{La}_2\text{NiO}_{4.133}$  for  $E \parallel \theta_0$  (solid line) and  $E \parallel \theta_0 + \frac{\pi}{2}$  (dashed line), compared with the  $c$ -axis loss function. The antiresonant features for  $E \parallel \theta_0 + \frac{\pi}{2}$  occur at the same frequency as the peaks in the  $c$ -axis loss function, calculated from the experimentally determined  $c$ -axis dielectric constant, in agreement with the model results in the upper panel.

sample geometries. The  $E \parallel \theta_0$  polarization appears to coincide with an angle of incidence that compensates for the misorientation of the  $a$ - $b$  plane. This observation has also recently been discussed in terms of unusual features in the reflectance of  $\text{La}_{2-x}\text{Sr}_x\text{CuO}_4$ .<sup>67</sup>

\*Electronic address: homes@bnl.gov

<sup>1</sup>J. M. Tranquada, D. J. Buttrey, V. Sachan, and J. E. Lorenzo, Phys. Rev. Lett. **73**, 1003 (1994).

<sup>2</sup>V. Sachan, D. J. Buttrey, J. M. Tranquada, J. E. Lorenzo, and G. Shirane, Phys. Rev. B **51**, 12742 (1995).

<sup>3</sup>J. M. Tranquada, D. J. Buttrey, and V. Sachan, Phys. Rev. B **54**, 12318 (1996).

<sup>4</sup>J. M. Tranquada, in *Neutron Scattering in Layered Copper-Oxide Superconductors*, edited by A. Furrer (Kluwer, Dordrecht, 1998), p. 225.

<sup>5</sup>P. Wochner, J. M. Tranquada, D. J. Buttrey, and V. Sachan, Phys. Rev. B **57**, 1066 (1998).

<sup>6</sup>H. Yoshizawa, T. Kakeshita, R. Kajimoto, T. Tanabe, T. Katsufuji, and Y. Tokura, Phys. Rev. B **61**, R854 (2000).

<sup>7</sup>M. E. Ghazi, P. D. Spencer, S. B. Wilkins, P. D. Hatton, D. Manix, D. Prabhakaran, A. T. Boothroyd, and S.-W. Cheong, Phys. Rev. B **70**, 144507 (2004).

<sup>8</sup>N. Ichikawa, S. Uchida, J. M. Tranquada, T. Niemöller, P. M. Gehring, S.-H. Lee, and J. R. Schneider, Phys. Rev. Lett. **85**, 1738 (2000).

<sup>9</sup>X. X. Bi, P. C. Eklund, E. McRae, J. G. Zhang, P. Metcalf, J. Spalek, and J. M. Honig, Phys. Rev. B **42**, 4756 (1990).

<sup>10</sup>T. Ido, K. Magoshi, H. Eisaki, and S. Uchida, Phys. Rev. B **44**, 12094 (1991).

- <sup>11</sup>X. X. Bi and P. C. Eklund, Phys. Rev. Lett. **70**, 2625 (1993).
- <sup>12</sup>X. X. Bi, P. C. Eklund, and J. M. Honig, Phys. Rev. B **48**, 3470 (1993).
- <sup>13</sup>D. A. Crandles, T. Timusk, J. D. Garret, and J. E. Greedan, Physica C **216**, 94 (1993).
- <sup>14</sup>D. M. Eagles, R. P. S. M. Lobo, and F. Gervais, Phys. Rev. B **52**, 6440 (1995).
- <sup>15</sup>T. Katsufuji, T. Tanabe, T. Ishikawa, Y. Fukuda, T. Arima, and Y. Tokura, Phys. Rev. B **54**, R14230 (1996).
- <sup>16</sup>P. Calvani, A. Paolone, P. Dore, S. Lupi, P. Maselli, P. G. Medaglia, and S. W. Cheong, Phys. Rev. B **54**, R9592 (1996).
- <sup>17</sup>B. Bäuml, G. Wellein, and H. Fehske, Phys. Rev. B **58**, 3663 (1998).
- <sup>18</sup>G. Blumberg, M. V. Klein, and S.-W. Cheong, Phys. Rev. Lett. **80**, 564 (1998).
- <sup>19</sup>K. Tsutsui, W. Koshibae, and S. Maekawa, Phys. Rev. B **59**, 9729 (1999).
- <sup>20</sup>T. Katsufuji, T. Tanabe, T. Ishikawa, S. Yamanouchi, Y. Tokura, T. Kakeshita, R. Kajimoto, and H. Yoshizawa, Phys. Rev. B **60**, R5097 (1999).
- <sup>21</sup>Y. G. Pashkevich, V. A. Blinkin, V. P. Gnezdilov, V. V. Tsapenko, V. V. Eremenko, P. Lemmens, M. Fischer, M. Grove, G. Güntherodt, L. Degiorgi *et al.*, Phys. Rev. Lett. **84**, 3919 (2000).
- <sup>22</sup>J. H. Jung, D.-W. Kim, T. W. Noh, H. C. Kim, H.-C. Ri, S. J. Levett, M. R. Lees, D. M. Paul, and G. Balakrishnan, Phys. Rev. B **64**, 165106 (2001).
- <sup>23</sup>C. H. Chen, S.-W. Cheong, and A. S. Cooper, Phys. Rev. Lett. **71**, 2461 (1993).
- <sup>24</sup>S.-W. Cheong, H. Y. Hwang, C. H. Chen, B. Batlogg, L. W. Rupp, and S. A. Carter, Phys. Rev. B **49**, 7088 (1994).
- <sup>25</sup>K. Yamamoto, T. Katsufuji, T. Tanabe, and Y. Tokura, Phys. Rev. Lett. **80**, 1493 (1998).
- <sup>26</sup>J.-M. Bassat, P. Odier, and F. Gervais, Phys. Rev. B **35**, 7126 (1987).
- <sup>27</sup>D. E. Rice, M. K. Crawford, D. J. Buttrey, and W. E. Farneth, Phys. Rev. B **42**, 8787 (1990).
- <sup>28</sup>G. Burns, F. H. Dacol, D. E. Rice, D. J. Buttrey, and M. K. Crawford, Phys. Rev. B **42**, 10777 (1990).
- <sup>29</sup>S. Tajima, T. Ido, S. Ishibashi, T. Itoh, H. Eisaki, Y. Mizuo, T. Arima, H. Takagi, and S. Uchida, Phys. Rev. B **43**, 10496 (1991).
- <sup>30</sup>N. Poirrot-Reveau, P. Odier, P. Simon, and F. Gervais, Phys. Rev. B **65**, 094503 (2002).
- <sup>31</sup>J. M. Tranquada, J. E. Lorenzo, D. J. Buttrey, and V. Sachan, Phys. Rev. B **52**, 3581 (1995).
- <sup>32</sup>C. C. Homes, J. M. Tranquada, Q. Li, A. R. Moodenbaugh, and D. J. Buttrey, Phys. Rev. B **67**, 184516 (2003).
- <sup>33</sup>D. E. Rice and D. J. Buttrey, J. Solid State Chem. **105**, 197 (1993).
- <sup>34</sup>J. D. Jorgensen, B. Dabrowski, S. Pei, D. R. Richards, and D. G. Hinks, Phys. Rev. B **40**, 2187 (1989).
- <sup>35</sup>G. H. Lander, P. J. Brown, J. Spátek, and J. M. Honig, Phys. Rev. B **40**, 4463 (1989).
- <sup>36</sup>T. Freltoft, D. J. Buttrey, G. Aeppli, D. Vaknin, and G. Shirane, Phys. Rev. B **44**, 5046 (1991).
- <sup>37</sup>J. M. Tranquada, Y. Kong, J. E. Lorenzo, D. J. Buttrey, D. E. Rice, and V. Sachan, Phys. Rev. B **50**, 6340 (1994).
- <sup>38</sup>C. C. Homes, M. Reedyk, D. Crandles, and T. Timusk, Appl. Opt. **32**, 2972 (1993).
- <sup>39</sup>M. Reedyk and T. Timusk, Phys. Rev. Lett. **69**, 2705 (1992).
- <sup>40</sup>J. H. Kim, B. J. Feenstra, H. S. Somal, D. van der Marel, W. Y. Lee, A. M. Gerrits, and A. Wittlin, Phys. Rev. B **49**, 13065 (1994).
- <sup>41</sup>T. Startseva, T. Timusk, M. Okuya, T. Kimura, and K. Kishio, Physica C **321**, 135 (1999).
- <sup>42</sup>A. A. Tsvetkov, D. Dulić, D. van der Marel, A. Damascelli, G. A. Kaljushnaia, J. I. Gorina, N. N. Senturina, N. N. Kolesnikov, Z. F. Ren, J. H. Wang *et al.*, Phys. Rev. B **60**, 13196 (1999).
- <sup>43</sup>A. Lucarelli, S. Lupi, M. Ortolani, P. Calvani, P. Maselli, M. Capizzi, P. Giura, H. Eisaki, N. Kikugawa, T. Fujita *et al.*, Phys. Rev. Lett. **90**, 037002 (2003).
- <sup>44</sup>S. Tajima, S. Uchida, D. van der Marel, and D. N. Basov, Phys. Rev. Lett. **91**, 129701 (2003).
- <sup>45</sup>A. Lucarelli, S. Lupi, M. Ortolani, P. Calvani, P. Maselli, and M. Capizzi, Phys. Rev. Lett. **91**, 129702 (2003).
- <sup>46</sup>S. Tajima, Y. Fudamoto, T. Kakeshita, B. Gorshunov, V. Zelezný, K. M. Kojima, M. Dressel, and S. Uchida, Phys. Rev. B **71**, 094508 (2005).
- <sup>47</sup>L. Pintschovius, J. M. Bassat, P. Odier, F. Gervais, G. Chevrier, W. Reichardt, and F. Gompf, Phys. Rev. B **40**, 2229 (1989).
- <sup>48</sup>L. Pintschovius, W. Reichardt, M. Braden, G. Dhalenne, and A. Revcolevschi, Phys. Rev. B **64**, 094510 (2001).
- <sup>49</sup>K. Yamamoto, K. Ishizaka, E. Saitoh, S. Shinomori, T. Tanabe, T. Katsufuji, and Y. Tokura, Phys. Rev. B **67**, 014414 (2003).
- <sup>50</sup>K. Ishizaka, Y. Taguchi, R. Kajimoto, H. Yoshizawa, and Y. Tokura, Phys. Rev. B **67**, 184418 (2003).
- <sup>51</sup>N. Poirrot, V. T. Phuoc, G. Gruener, and F. Gervais, Solid State Sci. **7**, 1157 (2005).
- <sup>52</sup>J. M. Tranquada, P. Wochner, A. R. Moodenbaugh, and D. J. Buttrey, Phys. Rev. B **55**, R6113 (1997).
- <sup>53</sup>F. D. Murnaghan, Am. J. Math. **49**, 235 (1937).
- <sup>54</sup>K. Parlinski, Z.-Q. Li, and Y. Kawazoe, Phys. Rev. Lett. **78**, 4063 (1997).
- <sup>55</sup>D. J. Singh, *Planewaves, Pseudopotentials and the LAPW Method* (Kluwer Academic, Boston, 1994).
- <sup>56</sup>D. Singh, Phys. Rev. B **43**, 6388 (1991).
- <sup>57</sup>P. Blaha, K. Schwarz, G. K. H. Madsen, D. Kvasnicka, and J. Luitz, WIEN2k, *An Augmented Plane Wave Plus Local Orbitals Program for Calculating Crystal Properties* (Techn. Universität Wien, Austria, 2001).
- <sup>58</sup>K. Parlinski, software PHONON, 2003.
- <sup>59</sup>J. M. Tranquada, K. Nakajima, M. Braden, L. Pintschovius, and R. J. McQueeney, Phys. Rev. Lett. **88**, 075505 (2002).
- <sup>60</sup>P. J. Heaney, A. Mehta, G. Sarosi, V. E. Lamberti, and A. Navrotsky, Phys. Rev. B **57**, 10370 (1998).
- <sup>61</sup>M. J. Rice, Phys. Rev. Lett. **37**, 36 (1976).
- <sup>62</sup>S. M. Shapiro (private communication).
- <sup>63</sup>D. van der Marel, J. H. Kim, B. J. Feenstra, and A. Wittlin, Phys. Rev. Lett. **71**, 2676 (1993).
- <sup>64</sup>R. M. A. Azzam and N. M. Bashara, *Ellipsometry and Polarized Light* (North-Holland, Amsterdam, 1987).
- <sup>65</sup>Fits to the electronic continuum at 295 K yield a Drude (zero-frequency) component of  $\omega_{pd}=2841$  and  $\Gamma=706\text{ cm}^{-1}$ ; in addition an overdamped midinfrared band has been employed to describe the midinfrared response with  $\omega_{MIR}=4126$ ,  $\gamma_{MIR}=11\,100$ , and  $\omega_{p,MIR}=17\,650\text{ cm}^{-1}$ .
- <sup>66</sup>D. W. Berreman, Phys. Rev. B **1**, 381 (1970).
- <sup>67</sup>M. Ortolani, P. Calvani, S. Lupi, P. Maselli, M. Fujita, and K. Yamada, J. Opt. Soc. Am. B **22**, 1994 (2005).